The signature of the tropospheric gravity wave background in observed mesoscale motion

Claudia Christine Stephan[1] and Alexis Mariaccia[2,*]

[1]Max Planck Institute for Meteorology, Hamburg, Germany
[2]Université Claude Bernard Lyon 1, Villeurbanne, France
[*]Now at Laboratoire Atmosphères, Observations Spatiales, Guyancourt, France

Correspondence: Claudia Christine Stephan (claudia.stephan@mpimet.mpg.de)

Abstract. How convection couples to mesoscale vertical motion and what determines these motions is poorly understood. This study diagnoses profiles of area-averaged mesoscale divergence from measurements of horizontal winds collected by an extensive upper-air sounding network of a recent campaign over the western tropical North Atlantic, the Elucidating the Role of Clouds-Circulation Coupling in Climate (EUREC[4]A) campaign. Observed area-averaged divergence amplitudes scale

5 approximately inversely with area equivalent radius. This functional dependence is also confirmed in reanalysis data and a global freely-evolving simulation run at 2.5 km horizontal resolution. Based on the numerical data it is demonstrated that the energy spectra of inertia gravity waves can explain the scaling of divergence amplitudes with area. At individual times, however, few waves can dominate the region. Nearly monochromatic tropospheric waves are diagnosed in the soundings by means of an optimized hodograph analysis. For one day, results suggest that an individual wave directly modulated the satellite-

10 observed cloud pattern. However, because such immediate wave impacts are rare, the systematic modulation of vertical motion due to inertia-gravity waves may be more relevant as a convection-modulating factor. The analytic relationship between energy spectra and divergence amplitudes proposed in this article, if confirmed by future studies, could be used to design better external forcing methods for regional models.

1 Introduction

The effects of large-spatial and long-time scale processes on convection are well understood, such as shallow convection prevailing in geographic locations of free-tropospheric subsidence associated with the Hadley cell (e.g., Albrecht et al., 1995; Norris, 1998; Wood and Hartmann, 2006). These links between convective regimes and circulation averaged over seasonal timescales are often the basis for prescribing an external forcing in limited-area models (Albrecht et al., 1979; Sobel and

20 Bretherton, 2000; van der Dussen et al., 2016). Cloudiness in conventional climate models is highly sensitive to the seasonal and synoptic-scale variations in the atmospheric state, but clouds do not vary adequately on time scales shorter than a day (e.g., Nuijens et al., 2015). Whereas models struggle to capture sub-daily cloud variability, which is pronounced on scales

of a few tens to several hundreds of kilometers, several observational studies have established direct links between sub-daily variability of cloudiness and mesoscale, i.e. $\mathcal{O}(100)$ km, vertical motion. For instance, Vogel et al. (2020) found that the

25 shallow convective mass flux is regulated primarily by mesoscale vertical motion at cloud base. George et al. (2020) showed that lower tropospheric mesoscale vertical velocity explains a larger fraction of variations in cloud base cloud fraction than local humidity or stability. Mauger and Norris (2010) reported variations in near-surface divergence to be the most important driver of cloud cover in the subtropical northeast Atlantic on time scales shorter than 12 h, whereas boundary layer stratification was relevant for time scales of 12–48 h. Their study relied on satellite observations as well as on reanalysis data to complement

30 the meteorological fields. The still relatively poor understanding of how clouds couple to circulation on scales of 20–200 km was the main motivation for recent efforts to design observations to measure the vertical profiles of area-averaged divergence on sub-daily timescales (e.g., Bony et al., 2017).

By deriving vertical profiles of divergence from sondes dropped along circular flight paths of 200 km diameter, Bony and Stevens (2019) showed that wave-like structures with vertical wavelengths of several kilometers, autocorrelations of multiple

35 hours, and amplitudes of the order of $2\times10^{-5}\mathrm{s}^{-1}$ dominated the divergence structure in the free troposphere over the tropical Atlantic. Stephan et al. (2020a) confirmed such features in soundings from the 2006 Tropical Warm Pool-International Cloud Experiment (TWP-ICE; May et al., 2008), which took place near Darwin, Australia. Furthermore, they tested if the characteristics of divergence variability might be consistent with the gravity wave dispersion relation, and concluded that gravity waves may serve to explain the temporal, vertical, and horizontal variability observed in area-averaged horizontal divergence. Their

40 study, however, is limited in two ways. First, they only diagnosed the average properties of gravity waves passing the domain, but not how variable the wave characteristics were. And secondly, the TWP-ICE campaign, as well as the circle flights of Bony and Stevens (2019), used constant-sized areas with a diameter of about 200 km, and thus could not be used to quantify the dependence of divergence characteristics on area size.

In this study we analyze the extensive radiosounding network (Stephan et al., 2020b) of the EUREC⁴A campaign (Stevens et

45 al., 2020). A network composed of a station at Barbados, four ships and two aircraft collected more than 2700 vertical profiles of winds, temperature and relative humidity over the course of 33 days. Since the ships were moving, this network sampled area-averaged divergence over different-sized regions. We derive area-averaged divergence using a three-dimensional variational analysis (described in Section 2.2). Independently of this, we diagnose the properties of gravity waves by applying a hodograph analysis to the horizontal winds measured by radiosondes (described in Section 2.3).

50 One aim of the present study is to interpret the properties of mesoscale divergence variability in the context of the tropospheric background wave spectrum, which we diagnose from the ERA5 reanalysis (Hersbach et al., 2020) and a global 2.5 km horizontal-resolution simulation initialized on the starting date of the campaign. It is well-known that the global kinetic energy spectrum follows a k^{-3} power law at synoptic scales of 1000–4000 km (e.g., Boer and Shepherd, 1983), which is related to slow balanced dynamics, and a $k^{-5/3}$ power law at mesoscales (e.g., Nastrom and Gage, 1985), which is mostly

55 associated with fast unbalanced dynamics and divergence. Hence, one may expect a link between the spectral characteristics of the global energy spectrum and the characteristics of regional area-averaged divergence. A related question is to what extent the tropospheric wave background at given times and locations is saturated versus being dominated by nearly monochromatic

waves. Several case studies have shown that individual gravity waves can organize convection (e.g., Shige and Satomura, 2001; Stechmann and Majda, 2009; Lane and Zhang, 2011). Therefore, a second aim of this study is to extract the properties of individual gravity waves from the soundings to quantify their variability, and to test if there are any direct wave imprints visible in patterns of convection.

In Section 2 we describe the observations, numerical data, and the methods of our analyses. The questions if and how global energy spectra are linked to mesoscale divergence are discussed in Section 3.1, whereas Section 3.2 focuses on local waves at specific times. Results are summarized and discussed in Section 4.

2 Data and methods

2.1 Observational data

To discuss potential links between vertical profiles of mesoscale divergence and convection, we show images from the Geostationary Operational Environmental Satellite-16 (GOES-16), which is centered on 75.2° W. Infrared (10.3 μm, Band 13) images of the GOES-16 Advanced Baseline Imager (ABI; Schmit et al., 2017) are provided by NASA's Worldview application (https://worldview.earthdata.nasa.gov). Information on the cloud bottom and top levels derived from the GOES-16 ABI (NOAA, 2018) is distributed by the Langley SATCORPS group of NASA.

Diagnostics of mesoscale divergence and gravity wave characteristics are based on measurements of surface-launched radiosondes, and dropsondes released from aircraft, taken during the EUREC[4]A campaign in Jan and Feb, 2020. The experimental design of EUREC[4]A involved 85 dropsonde circles from aircraft flights and regular releases of surface-launched radiosondes from five platforms. A combined data set with 895 dropsonde soundings from DLR's HALO aircraft and 322 dropsonde soundings from NOAA's WP-3D is publicly available at TO-BE-ADDED. We use the quality controlled Level-2 data with a vertical resolution of 10 m. HALO's circle typically consisted of twelve sondes and is centered at ∼13.3° N, -57.7° E, with a diameter of 200 km, as shown in Fig. 1b. The WP-3D circles, of which there are only 14, were mostly flown further east at varying locations within 59–50° W, 11–16° N. HALO data cover the surface up to the flight level of 9 km, WP-3D data the surface up to lower and variable flight levels with a maximum altitude of 7 km. We ingest all available dropsonde and surface-launched soundings into a three-dimensional variational analysis (3D-Var; described in Section 2.2) to estimate the area-averaged divergence. A separate 3D-Var analysis is performed just on the HALO circles to estimate divergence on this smaller scale.

In addition to using them in 3D-Var, we analyze Level-2 surface-launched soundings for gravity waves. These data, which cover the ground to the stratosphere (typically 25 km) in steps of 10 m, are described in Stephan et al. (2020b) and are publicly available at https://doi.org/10.25326/62. Unlike the circle flights, the continuous data coverage allows us to filter them in time to a specific frequency interval, as we describe in Section 2.3. These radiosondes were launched regularly (usually 4-hourly) from a network consisting of the Barbados Cloud Observatory (BCO) and four ships within 60–51° W, 6–16° N: the *R/V L'Atalante*, *R/V MS-Merian*, *R/V Meteor* and *R/V RH-Brown*. From Jan 8 to Feb 19, the network launched a total of 848 radiosondes from the surface and also recorded the descent for 82% of them. Since a typical ascent took about 90 min, this resulted

in high-frequency coverage during normal operations. The *Meteor* remained nearly stationary at a longitude of $57°$ W and moved north- and southward between 12.0–$14.5°$ N. The *RH-Brown* moved approximately orthogonal to *Meteor's* sampling line between the BCO ($59.43°$ W, $13.16°$ N) and the Northwest Tropical Atlantic Station for air-sea flux measurements buoy (NTAS) at $51.02°$ W, $14.82°$ N. The *MS-Merian* and *Atalante* ventured further to the south to a minimum latitude of $\sim 6.5°$ N

95 and were often in close proximity, i.e. < 200 km apart. The ships' routes are displayed in Fig. 2 of Stephan et al. (2020b).

2.2 3D variational analysis

The computation of divergence and vorticity from sounding data is performed with an analysis tool called 3D-Var, described in López Carrillo and Raymond (2011). It ingests spatially nonuniform profiles of temperature, horizontal wind, mixing ratio and pressure, and interpolates them onto a regular grid of the user's choice. Following a weighted least squares algorithm, 3D-Var

100 then minimizes the misfit between the computed fields and the gridded input measurements. This minimization problem is additionally constrained by the anelastic mass continuity equation. We use a $0.5° \times 0.5°$ longitude-latitude grid for analyzing data from the full network of soundings, and a $0.1° \times 0.1°$ longitude-latitude grid for our separate analysis of data from HALO's circle flights. Since we are interested in variability on vertical scales >1 km, a vertical grid spacing of 200 m is chosen, covering the surface up to 16 km.

105 3D-Var is applied every hour between Jan 18 and Feb 16 (720 hours). From the analysis of Bony and Stevens (2019) divergence autocorrelations for the HALO circles are expected to exceed 3 hours, and to increase with the area over which divergence is averaged. Therefore, to improve data density, we ingest, for each given time, data within $\pm(\Delta t = 90$ min$)$. This choice results in nearly continuous 3D-Var results between Jan 18 and Feb 16, as can be seen in Fig. 1a, which shows the equivalent radius, computed as $R = \sqrt{A/\pi}$. The area A, in which the data assimilation is performed, is limited to the region

110 with good data coverage, to avoid extrapolation. For each application of 3D-Var, this area is defined by the boundaries of a polygon that encloses all available soundings and whose corners are grid points with full vertical coverage in all variables. For Jan 31, Fig. 1b shows an example of such a polygon. The blue polygon is the mask for the $0.5° \times 0.5°$ all-soundings assimilation, and the red triangles mark the polygon bounds of the $0.1° \times 0.1°$ HALO-circle assimilation. We discard all times at which the aspect ratio of a polygon's perimeter L and the equivalent radius R (as defined above) is $L/R < 2$, to limit the

115 analysis to areas with little distortion. For the blue polygon in Fig. 1b, for instance, $L/R = 1.3$. The output of 3D-Var contains the 3D fields of divergence and vorticity within the polygon bounds. We average them horizontally to compute vertical profiles of divergence and vorticity.

2.3 Hodograph analysis

The hodographs of the horizontal wind perturbations associated with low-frequency gravity waves describe ellipses whose

120 properties can be determined using the Stokes parameters, as in Eckermann and Vincent (1989). Properties that follow immediately are the ratio of the minor to the major axis, ϵ, the orientation of the major axis relative to the zonal direction, Θ, and the degree of polarization of the ellipse, d. Large d indicate that a sounding contains coherent waves rather than noise. Therefore,

we iteratively search for time-altitude windows in the radiosonde measurements that give large values of d, as described in the following.

125   We analyze data from each platform separately, with one exception: over the studied period, the *MS-Merian* launched fewer radiosondes (118) than the others ships (203 *Meteor*, 169 *RH-Brown*), which was partly due to her proximity to the *Atalante* (139 radiosondes). Thus, to achieve continuous data coverage we include selected soundings collected by the *MS-Merian* with those of the *Atalante*; specifically, soundings of the *MS-Merian* that were taken within 100 km of the *Atalante* are added to the *Atalante's* dataset. This choice is reasonable as the drift of a sonde can be of the order of 100 km. From now on, we will

130   refer to this merged dataset as the Combined dataset. The BCO is the only spatially fixed platform. They launched 182 sondes, whose horizontal wind measurements from Jan 21 at 0200 UTC to Feb 17 at 1200 UTC are shown in Fig. 2a,b.

Missing values in each dataset are filled by interpolating in time to a one-hourly resolution. A Lanczos filter is applied to horizontal winds and temperature profiles to retain vertical wavelengths of $500\,\mathrm{m} < \lambda_z < 10\,\mathrm{km}$ and periods of $3\,\mathrm{h} < \tau < 53$ h, where 53 h corresponds to the inertial period at the BCO. Figure 2c,d shows the resulting horizontal wind perturbations for

135   the BCO. Coherent structures are clearly visible in both wind components. Oftentimes they exhibit a downward propagation with time, which is characteristic of upward propagating gravity waves.

At each time we compute the quadrature spectrum between the zonal and meridional wind perturbations, $u'(z)$ and $v'(z)$. Then we search the resulting spectrum, which is a function of time and vertical wavenumber m, for local maxima in m that persist in time for at least 10 h. The vertical profiles of $u'(z)$ and $v'(z)$ are then filtered to include only the peak vertical

140   wavenumber and the adjacent wavenumbers. A first guess for the associated time window, $[t_s^0, t_e^0]$, is obtained from the positions of the adjacent minima. At this point, the vertical wavelength assigned to the event is determined from the power-weighted mean wavenumber of the selected time-wavenumber window. The initial altitude interval $[h_s^0, h_e^0]$ is $[0, 18]$ km. The degree of polarization d is next computed for the initial window and all possible combinations of shorter windows contained in it. The window defined by $[t_s, t_e]$, $[h_s, h_e]$, where $t_s^0 \leq t_s < t_e \leq t_e^0$ and $h_s^0 \leq h_s < h_e \leq h_e^0$, with the greatest total number of data

145   points and a polarization $d \geq 0.8$ is saved for subsequent analysis. If no window inside $[t_s^0, t_e^0]$, $[h_s^0, h_e^0]$ with $d \geq 0.8$ can be found, then the peak is discarded. Otherwise ϵ and Θ are computed using the Stokes parameters.

The angle Θ of the major axis of the ellipse counter-clockwise from the eastward direction is the direction of wave propagation, but with an ambiguity of $180°$. To resolve this ambiguity we also compute this angle as in Evan and Alexander (2008):

150    $$\Theta_{T'_{+90}} = \tan^{-1}\left(\frac{\overline{u'T'_{+90}}}{\overline{v'T'_{+90}}}\right),$$

(1)

where T'_{+90} is the value of the temperature perturbation after shifting the phase by $+90°$ using a Hilbert transform. Finally, the ratio ϵ of the minor to the major axis is related to the intrinsic frequency Ω of the gravity wave as

$$\epsilon = \frac{f}{\Omega} - \frac{k_h m \overline{V_z}}{[m^2 + 1/(4H_s^2)]\Omega},$$

(2)

where f is the Coriolis parameter, H_s the density scale height, k_h the magnitude of the horizontal wave number vector and

155    $\overline{V_z} = \overline{(\mathrm{d}V/\mathrm{d}z)}$ the mean shear of the horizontal wind in the direction perpendicular to Θ. To compute $\overline{V_z}$ we first average V over $[h_s, h_e]$ and $[t_s, t_e]$.

The dispersion relation for inertia-gravity waves (e.g., Hankinson et al., 2014), is

$$\Omega^2 = f^2 + \frac{N^2 k_h^2}{m^2 + 1/(4H_s^2)} - \frac{2f k_h m \overline{V}_z}{m^2 + 1/(4H_s^2)}, \tag{3}$$

where N is the Brunt-Väisälä frequency. Combining (2) with (3) gives

160    $$\Omega^2 (\epsilon^2 - a^2) - 2\Omega f \epsilon (1 - a^2) + f^2 (1 - a^2) = 0, \tag{4}$$

where $a^2 = \overline{V_z^2}/(N^2 [1 + (4m^2 H_s^2)^{-1}])$. Solving for $\frac{\Omega}{f}$, this results in

$$\frac{\Omega}{f} = \frac{\epsilon \left(1 - a^2\right) \pm \left[\epsilon^2 \left(1 - a^2\right)^2 - \left(\epsilon^2 - a^2\right)\left(1 - a^2\right)\right]^{1/2}}{\epsilon^2 - a^2}. \tag{5}$$

After determining Ω, k_h follows from the rearranged dispersion relation (3):

$$k_h = k_{\mathrm{disp}} = \frac{f m \overline{V_z}}{N^2} \pm \frac{1}{N} \left[\frac{f^2 m^2}{N^2} \overline{V_z}^2 + \left(\Omega^2 - f^2\right)\left(m^2 + \frac{1}{4H_s^2}\right) \right]^{1/2}, \tag{6}$$

165   where by definition k_h is positive in the direction of wave propagation.

To obtain the ground-based frequency ω we compute at each altitude the quadrature spectrum between $u'(t)$ and $v'(t)$, $QS(t, \nu)$, using the S-transformation (Stockwell et al., 1996):

$$QS(z; t, \nu) = \Im[ST_u(t, \nu) \cdot ST_v^*(t, \nu)]|_z \tag{7}$$

where $ST_u(t, \nu)$ is the S-transformation in the time dimension of $u'(t)$ at a given z, and ν denotes frequency. Then, ω corre-

170   sponds to the peak in $QS(z; t, \nu)$ after integrating over $[h_s, h_e]$ and $[t_s, t_e]$.

In principle we could estimate ω from the background wind in the direction of wave propagation, U_h, using $\omega = \Omega + k_h U_h$. However, due to the strong wind shear (see Fig. 2a,b), these results would be highly sensitive to the altitude range selected to compute U_h. As the Doppler shift equation assumes $U_h(z) = const$, it is not clear if U_h is best approximated as an average across an altitude range or the wind at a particular level. Moreover, as U_h is the projection of the horizontal wind along the

175   wave propagation direction, an additional uncertainty is introduced by the uncertainty in Θ. For this reason we compute ω with the alternative method described above.

2.4   Normal mode decomposition of numerical data

We derive global wave spectra as well as vertical profiles of regionally-averaged divergence and vorticity from the ERA5 reanalysis and a numerical simulation. For both data sets we analyze 3-hourly horizontal winds between Jan 20 – Feb 29, 2020,

180   matching the EUREC[4]A period.

ERA5 is produced and made publicly available by the European Centre for Medium Range Weather Forecasts (ECMWF). The original data with a horizontal resolution of ∼30 km are stored on 137 hybrid sigma/pressure levels from the surface up to an altitude of 80 km (0.01 hPa).

The numerical simulation run at 2.5 km horizontal resolution is performed with the ICON model (Zängl et al., 2015). It was initialized at 0000 UTC on Jan 20, 2020 from an operational analysis of the atmospheric state produced by the ECMWF and forced at the lower boundary with 5-day running-mean sea surface temperatures, which are also taken from an ECMWF analysis. 90 vertical levels extend from the surface up to 75 km with a Klemp-type implicit Rayleigh damping (Klemp et al., 2008) of vertical winds starting at 44 km. The simulation is freely evolving and integrated until 0000 UTC on Mar 1, 2020.

We re-grid the data from both ERA5 and ICON to a regular n256 Gaussian grid with 1024×512 points in longitude and latitude, respectively, corresponding to a resolution of 39 km at the equator. In the vertical we interpolate to 68 hybrid sigma/pressure levels between the surface and 10 hPa (∼31 km).

The data at each time step are then subjected to a normal-mode function decomposition, using the freely-available software package MODES, a detailed description of which is given in Žagar et al. (2015). The modal decomposition projects the three-dimensional fields of geopotential height and horizontal wind onto an orthogonal set of basis functions. These functions are solutions to the Rossby and inertia-gravity wave (IG) dispersion relationships, respectively (Kasahara, 1976). Since the former are vorticity-dominated we label them as ROT. The orthogonality of the basis functions allows filtering out specific wave modes, including the option of a subsequent inversion back to physical space. This allows us to derive the local wind fields inside the EUREC[4]A domain, as well as corresponding divergence and vorticity fields, associated with specific modes.

3 Results

3.1 Effects of the global wave spectrum on mesoscale divergence

Figure 3a,b shows how vertical profiles of area-averaged divergence vary in time. The strong vertical variability in the profiles derived from the array of all soundings and the circle, respectively, is consistent with previous observations by Bony and Stevens (2019) and Stephan et al. (2020a). Vorticity varies on longer scales in time-altitude space (Fig. 3c,d). For ERA5 and ICON we display the corresponding divergence and vorticity profiles associated with IG and ROT modes, respectively (Fig. 4). These profiles are computed for the same geographical region and an equivalent radius of ∼260 km. This radius corresponds to the smallest radius that allows us to compute a centered area-average, i.e. using odd numbers of grid points in each direction on the n256 Gaussian grid, while at the same time exceeding the truncation scales applied in the normal mode decomposition in both horizontal directions (truncation meridonal wavenumber $n = 200$; zonal wavenumber $k = 320$). Divergence associated with ROT modes is negligible; ROT modes possess only 2.4% (ERA5) and 3.3% (ICON) of the variance contained in the IG modes of Fig. 4a,b. Similarly, IG modes possess only 3.8% (ERA5) and 3.1% (ICON) of the variance contained in the ROT modes of Fig. 4c,d. Figure 4 also shows strong variability at short scales in divergence and at long scales in vorticity, respectively, with similar magnitudes as observed. Notably, 3D-Var, which ingests a 3-hour running-mean of measurements, as well as MODES, which is independently applied at single time steps, yield divergence as well as vorticity anomalies that

exhibit temporal persistence with vertically coherent structures. From the comparison between observations and numerical data

215 we conclude that by far the largest fraction of divergence variability inside the sounding network is due to IG waves.

Because the EUREC[4]A sounding network sampled areas of different sizes, we can for the first time address how observed magnitudes of area-averaged divergence variability change with area. Figure 5 shows scatter plots of divergence amplitudes multiplied by the corresponding area equivalent radius versus the equivalent radius for three different tropospheric layers. We here define divergence amplitude as the difference between the maximum and minimum value found in a layer. The running

220 means (thick dots) follow lines that are approximately horizontal, albeit with a slight upward slope at $h = 6$–9 km. Thus, divergence amplitudes at equivalent radii of 100–300 km scale approximately inversely with radius.

ERA5 and ICON also show such an inverse scaling of divergence amplitudes (Fig. 6). As expected from the predominant IG contribution to divergence, this scaling is due to the scaling of the IG-driven divergence field. While the lower bound in R is limited by our choice of normal mode expansion parameters, we can compute divergence for areas that exceed the sizes

225 sampled during EUREC[4]A. Figure 6 shows that the approximate R^{-1}-scaling of divergence amplitudes remains valid across the entire mesoscale, up to at least the synoptic scale of about 1000 km (zonal wavenumber 38). ERA5 and ICON produce qualitatively similar results, but we notice in Fig. 6 that ERA5 has slightly larger divergence amplitudes than ICON. To shed light on this difference, and, more importantly, to find an explanation for the scaling with radius, Fig. 7 examines the global energy spectra in ERA5 and ICON and their decomposition into IG and ROT modes.

230 In both data sets the total energy follows a k^{-1} power law at synoptic scales that transitions to a steeper slope at $k \approx 8$. For $k > 8$ the ROT spectrum in ERA5 scales as k^{-3}, and the IG spectrum follows on average a $k^{-5/3}$ slope but with substantial deviations from a constant slope. Towards the largest k there is a further steepening in ERA5, which was also reported for ERA-Interim and points to a lack of energy at small scales in the reanalysis (Žagar et al., 2015). The spectral behavior in ICON is similar to ERA5, but the slopes for different regimes are more sharply defined. The IG curve follows a $k^{-1/2}$ slope for $k < 8$,

235 then $k^{-5/3}$ up to $k \approx 100$. At $k > 100$, there is a slight steepening in ICON as well, such that the slope between $k \approx 100$–150 is k^{-2}. The smallest scale shown in Fig. 6 is $k = 150$; the R–range of Fig. 6 corresponds to k$\in [37, 150]$. The three prominent slopes of $k^{-1/2}$, $k^{-5/3}$ and k^{-2} are marked with magenta lines in Fig. 6b.

As it turns out, the spectral slopes can be used to predict the magenta lines in Fig. 6b, i.e. they can explain how divergence magnitudes vary with equivalent radius. Consider a gravity wave with wave vector (k, l, m), frequency ω and phase ϕ. The

240 associated wind perturbations can be expressed as

$$(u, v, w) = (A_x, A_y, A_z) \sin(kx + ly + mz - \omega t + \phi), \tag{8}$$

where the amplitudes A_i are functions of the wave vector. The associated horizontal divergence scales with k and l as follows:

$$\text{Div} \sim (kA_x + lA_y) \cos(kx + ly + mz - \omega t + \phi) \tag{9}$$

As we will demonstrate in Section 3.2, the IG waves inside the EUREC[4]A domain were mainly propagating zonally, so that

245 we can assume divergence to scale as $\text{Div} \sim kA_x(k)$. How $A_x(k)$ depends on k is contained in the identified spectral slopes of Fig. 7b: A_x scales as $k^{-1/4}$ for $k < 8$, as $k^{-5/6}$ for $k = 8$–100 and as k^{-1} for $k = 100$–150. To derive the relationship

between these spectral slopes and the divergence amplitudes, we follow the ansatz that each averaging scale $R^* = 2\pi/k^*$ feels the divergence on all scales $R > R^*$, whereas divergence at scales $R < R^*$ has little or no effect. Under this assumption, the scaling of divergence amplitudes $A_D(k^*)$ can be approximated by the sum over all k smaller or equal to $k^* = 2\pi/R^*$:

$$A_D(k^*) \sim \sum_{k=1}^{k=k^*} k \cdot A_x(k) \sim \sum_{k=1}^{k=k^*} k \cdot k^{\sigma(k)}, \tag{10}$$

with $\sigma(k) \in \{-1/4, -5/6, -1\}$, as indicated above. Computing this sum and multiplying by a constant to match the IG point at $R = 1044$ km in Fig. 6b,d,f results in the magenta lines drawn in these panels. Evidently, at 3–6 and 6–9 km altitude, the match is excellent. At 1–3 km Fig. 6f misses the decrease in divergence magnitude at small R. This might be due to an introduction of additional energy at short horizontal scales by convection, which tends to have tops at 1–2 km during EUREC^{4}A. The validity of (10) is further discussed in Section 4.

3.2 Effects of individual waves on mesoscale divergence

In the previous section we related the characteristics of the global IG spectrum to the statistical properties of variability in area-averaged mesoscale divergence. We can now explain divergence magnitudes in a statistical sense, but the longevity of structures identified in Figs 3 and 4 suggest that individual waves may dominate the local divergence field at many times. It is important to note that the result obtained in the previous section does not require a saturated wave spectrum. Evidently, the local spatio-temporal predominance of one or a few wave would change the scaling law in the given period and region, but this is consistent with the relatively large standard deviations in Figs 5 and 6. Therefore, we next investigate if the generic IG waves that appear to govern the statistics of mesoscale divergence can directly modulate convection through their individual impact on mesoscale vertical motion.

To study local wave characteristics, we use the iterative hodograph algorithm, which is designed specifically to detect nearly monochromatic waves in soundings (see Section 2.3). The algorithm extracted 34 wave events with polarization $d \geq 0.8$, and with an average polarization of 0.84. All events and extracted wave characteristics are listed in Table 1. Most detected waves have vertical wavelengths of 1.2–4 km with a mean of 2.6 km, and highly variable horizontal wavelengths with a mean and standard deviation of $\mathcal{O}(450)$ km. Intrinsic periods range from 6–45 h with a mean of 21 h, and ground-based periods from 11–50 h with a mean of 28 h. The average propagation direction, computed with two different methods, is eastward.

The identified wave characteristics do not show any evidence for systematic changes over the period of the campaign. This is consistent with a generally broad but unsaturated tropospheric IG background. If the wave background were saturated, then it would be impossible to identify waves with a high degree of polarization. Instead, at most times, we are able to find predominant waves (Table 1).

A day on which gravity waves most likely had an effect on the cloud field is Jan 31. Figure 8 shows hourly infrared satellite images of the campaign region on this day. A smooth modulation of the cloud field is clearly visible in the form of alternating southwest to northeast oriented bands of dry and cloudy areas. The crests of the cloudy areas are topped by narrow stripes of bright clouds. One of the larger cloud clusters seen in the images is located inside the HALO circle. The top and bottom height of this cloud are ∼2.3 km and ∼1 km, respectively. In the cloud layer the mean zonal wind is -4.3 m s^{-1} and the

280 mean meridional wind is -0.1 m s^{-1}. Thus, the motion of the cloud cluster across the circle (diameter of 200 km) matches the estimated advection of 100 km in 6.5 hours.

Jan 31 is also the day when the wave algorithm detected the most distinct wave event. Three out of the four data sets from the surface-based stations contain a wave signal with a high degree of polarization (0.86, 0.86, 0.87; Table 1). Notably, the three detected waves agree broadly in terms of the estimated horizontal wavelengths (480 km, 340 km, 440 km), which match

285 well the 400 km spacing of the respective moist or dry regions in Fig. 8. In addition, the long ground-based periods (33 h, 27 h, 34 h) are consistent with the nearly stationary appearance of the cloud field in Fig. 8.

The propagation direction indicated by the algorithm, however, is more due eastward (-14°, -28°, -11°) than one would expect from the alignment of the cloud pattern. It could be that vertical propagation and refraction of the wave are partly responsible for this difference, because the ships were located further to the south, where a patterning of clouds is not visible

290 (not shown). To obtain an additional estimate of wave parameters that allows for a more direct comparison with Fig. 8, we apply a hodograph analysis to the 66 HALO dropsonde profiles collected on Jan 31 over the course of multiple circle flights. Their locations are marked by red triangles in Fig. 8. We pre-select the altitude interval of 2–5 km in order to include the upper portion of the cloud layer while avoiding noise near the surface. Since the entire duration of the flight is less than 8 hours, we compute wind perturbations by removing the average of all profiles instead of filtering in time. The resulting horizontal

295 wavelength is 421 km with a propagation angle $\Theta = -43.1°$, in agreement with Fig. 8.

The good match of the satellite image with wave properties found independently in data from four stations is a strong indication for a causal link. Jan 31 was the only day that showed a potential wave imprint on the cloud field that was detectable by eye. Thus, we conclude that visible effects of individual waves on convection occur rather seldom, at least during boreal winter in the studied region.

4 Conclusions

This study extended the analysis of recent novel measurements of mesoscale divergence variability (Bony and Stevens, 2019) by diagnosing vertical profiles of mesoscale divergence in the extensive sounding network of the 2020 EUREC^{4}A field campaign. For the first time, we could measure how divergence magnitudes depend on the area over which averages are computed, which may be relevant to sub-daily variability of cloudiness (Mauger and Norris, 2010; Vogel et al., 2020; George et al., 2020).

305 Observed divergence magnitudes during EUREC^{4}A scale approximately inversely with the area equivalent radius, a result that is also true for the ERA5 reanalysis and a 2.5 km global numerical simulation. By applying a normal mode decomposition to the numerical data, we demonstrated that the major fraction of mesoscale divergence variability is due to inertia-gravity (IG) waves, confirming the hypothesis put forward by Stephan et al. (2020a).

Moreover, we derived an analytic relationship between the wave-number dependence of global IG energy spectra and the

310 scaling of divergence amplitudes with area. The essential ansatz for this equation (10) is that IG waves on all scales larger than a considered area contribute to the divergence averaged over this area. The data presented in this study follow equation (10) very closely. Yet, the relationship is not trivial from an intellectual point of view, as one might expect some cancellation of the

local divergence induced by some IG waves with the local convergence associated with other IG waves. Either this cancellation has no effect on the overall scaling of divergence amplitudes (note that equation (10) only predicts their scaling with area, not their absolute magnitude), or the cancellation is negligible. The second possibility is more likely to be true if the tropospheric IG wave background is not saturated, but locally composed of few waves. Persistent features in filtered-wind and divergence profiles suggest that the latter possibility may apply.

To gain more information about the properties of local waves, we extracted nearly monochromatic wave events from soundings by means of an iterative hodograph analysis. For most days, clear IG signals could be found, and on one day, the identified wave likely had a direct effect on the organization of clouds, as evidenced by comparison to satellite images. Thus, although seldom, direct wave imprints on convection do occur. This suggests that the IG wave background is indeed not saturated. However, the systematic modulation of vertical motion due to IG waves of different scales may be more relevant for convection. More research is required to quantify the relative importance of the stochastic wave forcing for shaping patterns of convection, compared to other well-known local influences such as, e.g., lower tropospheric stability (Medeiros and Stevens, 2011), relative humidity (Slingo, 1987) and sea surface temperature (Qu et al., 2015).

Future studies should repeat the measurements analyzed in this study for different regions, especially different latitudes, as well as regions over land, to test the universal applicability of the proposed relationship between energy spectra and divergence amplitudes. If confirmed, then our results imply that all scales are relevant for mesoscale variability, which has consequences for regional models that introduce an artificial truncation scale, and could be used to design better external forcing methods for regional models.

Author contributions. TEXT

C.C. Stephan conceptualized the study and prepared the manuscript. A. Mariaccia carried out the hodograph analysis and provided Fig. 2.

Competing interests. TEXT

There are no competing interests.

Acknowledgements. C.C. Stephan was supported by the Minerva Fast Track Programme of the Max Planck Society. She would like to thank Professor David Raymond for his help with the 3D-Var software, which is openly available for download at http://kestrel.nmt.edu/~raymond/software/candis/candis.html. She is also grateful to Professor Nedjeljka Žagar for her advice on using the MODES software, which can be obtained at https://modes.cen.uni-hamburg.de/download. The vertically gridded (Level-2) radiosounding data described by Stephan et al. (2020b) in NetCDF format are available to the public at https://doi.org/10.25326/62, and the corresponding dropsonde data at to-be-added. GOES-16 Advanced Baseline Imager data are provided by NASA's Worldview application (https://worldview.earthdata.nasa.gov). ERA5 is

produced and made publicly available by the European Centre for Medium Range Weather Forecasts (ECMWF). Data from the numerical simulation are stored by the Excellence in Science of Weather and Climate in Europe (ESiWACE) project at the German Climate Computing Center (DKRZ). The ICON source code is publicly available and associated primary data are stored at handle-to-be-added.

References

345

Albrecht, B. A., Betts, A. K., Schubert, W. H., and Cox, S. K.: Model of the thermodynamic structure of the trade-wind boundary layer: Part I. Theoretical formulation and sensitivity tests, J. Atmos. Sci., 36, 73–89, https://doi.org/10.1175/1520-0469(1979)036<0073:MOTTSO>2.0.CO;2, 1979.

Albrecht, B. A., Jensen, M. P., and Syrett, W. J.: Marine boundary layer structure and fractional cloudiness, J. Geophys. Res. Atmos., 100, 350 14 209–14 222, https://doi.org/https://doi.org/10.1029/95JD00827, 1995.

Boer, G. J. and Shepherd, T. G.: Large-scale two-dimensional turbulence in the atmosphere, J. Atmos. Sci., 40, 164–184, 1983.

Bony, S. and Stevens, B.: Measuring area-averaged vertical motions with dropsondes, J. Atmos. Sci., 76, 767–783, https://doi.org/10.1175/JAS-D-18-0141.1, 2019.

Bony, S., Stevens, B., Ament, F., Bigorre, S., Chazette, P., Crewell, S., Delanoë, J., Emanuel, K., Farrell, D., Flamant, C., Gross, S., Hirsch, 355 L., Karstensen, J., Mayer, B., Nuijens, L., Ruppert, J. H., Sandu, I., Siebesma, P., Speich, S., Szczap, F., Totems, J., Vogel, R., Wendisch, M., and Wirth, M.: EUREC4A: A field campaign to elucidate the couplings between clouds, convection and circulation, Surv. Geophys., 38, 1529–1568, https://doi.org/10.1007/s10712-017-9428-0, 2017.

Eckermann, S. D. and Vincent, R. A.: Falling sphere observations of anisotropic gravity wave motions in the upper stratosphere over Australia, Pure Appl. Geophys., 130, 509–532, https://doi.org/10.1007/BF00874472, 1989.

360 Evan, S. and Alexander, M. J.: Intermediate-scale tropical inertia gravity waves observed during the TWP-ICE campaign, J. Geophys. Res., 113, D14101, https://doi.org/10.1029/2007JD009289, 2008.

George, G., Stevens, B., Bony, S., Klingebiel, M., and Vogel, R.: Observed impact of meso-scale vertical motion on cloudiness, J. Atmos. Sci., under review, 2020.

Hankinson, M. C. N., Reeder, M. J., and Lane, T. P.: Gravity waves generated by convection during TWP-ICE: I. Inertia-gravity waves, J. 365 Geophys. Res. Atmos., 119, 5269–5282, https://doi.org/10.1002/2013JD020724, 2014.

Hersbach, H., Bell, B., Berrisford, P., Hirahara, S., Horányi, A., Muñoz-Sabater, J., Nicolas, J., Peubey, C., Radu, R., Schepers, D., Simmons, A., Soci, C., Abdalla, S., Abellan, X., Balsamo, G., Bechtold, P., Biavati, G., Bidlot, J., Bonavita, M., De Chiara, G., Dahlgren, P., Dee, D., Diamantakis, M., Dragani, R., Flemming, J., Forbes, R., Fuentes, M., Geer, A., Haimberger, L., Healy, S., Hogan, R. J., Hólm, E., Janisková, M., Keeley, S., Laloyaux, P., Lopez, P., Lupu, C., Radnoti, G., de Rosnay, P., Rozum, I., Vamborg, F., Villaume, S., and Thépaut, 370 J.-N.: The ERA5 global reanalysis, Quart. J. Roy. Meteor. Soc., 146, 1999–2049, https://doi.org/https://doi.org/10.1002/qj.3803, 2020.

Kasahara, A.: Normal modes of ultralong waves in the atmosphere, Mon. Wea. Rev., 104, 669–690, 1976.

Klemp, J. B., Dudhia, J., and Hassiotis, A. D.: An upper gravity-wave absorbing layer for NWP applications, Mon. Wea. Rev., 136, 3987–4004, https://doi.org/10.1175/2008MWR2596.1, 2008.

Lane, T. P. and Zhang, F.: Coupling between gravity waves and tropical convection at mesoscales, J. Atmos. Sci., 68, 2582–2598, 375 https://doi.org/10.1175/2011JAS3577.1, 2011.

López Carrillo, C. and Raymond, D. J.: Retrieval of three-dimensional wind fields from Doppler radar data using an efficient two-step approach, Atmos. Meas. Tech., 4, 2717–2733, https://doi.org/10.5194/amt-4-2717-2011, https://amt.copernicus.org/articles/4/2717/2011/, 2011.

Mauger, G. S. and Norris, J. R.: Assessing the impact of meteorological history on subtropical cloud fraction, J. Climate, 23, 2926–2940, 380 https://doi.org/10.1175/2010JCLI3272.1, 2010.

May, P. T., Mather, J. H., Vaughan, G., Jakob, C., McFarquhar, G. M., Bower, K. N., and Mace, G. G.: The Tropical Warm Pool-International
Cloud Experiment, Bull. Am. Meteorol. Soc., 89, 629–645, https://doi.org/10.1175/BAMS-89-5-629, 2008.

Medeiros, B. and Stevens, B.: Revealing differences in GCM representations of low clouds, Clim. Dyn., 36, 385—399,
https://doi.org/10.1007/s00382-009-0694-5, 2011.

385 Nastrom, G. D. and Gage, K. S.: A climatology of aircraft wavenumber spectra observed by commercial aircraft, J. Atmos. Sci., 42, 950–960,
1985.

NOAA: NOAA GOES-R series Advanced Baseline Imager (ABI) Level 2 cloud top height (ACHA). GOES-R algorithm working group, and
GOES-R series program office. NOAA national centers for environmental Information., https://doi.org/10.7289/V5HX19ZQ, 2018.

Norris, J. R.: Low cloud type over the ocean from surface observations. Part I: Relationship to surface meteorology and the vertical dis-
390 tribution of temperature and moisture, J. Climate, 11, 369–382, https://doi.org/10.1175/1520-0442(1998)011<0369:LCTOTO>2.0.CO;2,
1998.

Nuijens, L., Medeiros, B., Sandu, I., and Ahlgrimm, M.: The behavior of trade-wind cloudiness in observations and models: The major cloud
components and their variability, J. Adv. Mod. Earth Sys., 7, 600–616, https://doi.org/https://doi.org/10.1002/2014MS000390, 2015.

Qu, X., Hall, A., Klein, S. A., and DeAngelis, A. M.: Positive tropical marine low-cloud cover feedback inferred from cloud-controlling
395 factors, Geophys. Res. Lett., 42, 7767–7775, https://doi.org/https://doi.org/10.1002/2015GL065627, 2015.

Schmit, T. J., Griffith, P., Gunshor, M. M., Daniels, J. M., Goodman, S. J., and Lebair, W. J.: A closer look at the ABI on the GOES-R series,
Bull. Amer. Meteor. Soc., 98, 681–698, https://doi.org/10.1175/BAMS-D-15-00230.1, 2017.

Shige, S. and Satomura, T.: Westward generation of eastward-moving tropical convective bands in TOGA COARE, J. Atmos. Sci., 58,
3724–3740, https://doi.org/10.1175/1520-0469(2001)058<3724%3AWGOEMT>2.0.CO%3B2, 2001.

400 Slingo, J. M.: The development and verification of a cloud prediction scheme for the ECMWF model, Quart. J. Roy. Meteor. Soc., 113,
899–927, https://doi.org/https://doi.org/10.1002/qj.49711347710, 1987.

Sobel, A. H. and Bretherton, C. S.: Modeling tropical precipitation in a single column, J. Climate, 13, 4378–4392,
https://doi.org/10.1175/1520-0442(2000)013<4378:MTPIAS>2.0.CO;2, 2000.

Stechmann, S. N. and Majda, A. J.: Gravity waves in shear and implications for organized convection, J. Atmos. Sci., 66, 2579–2599,
405 https://doi.org/10.1175/2009JAS2976.1, 2009.

Stephan, C. C., Lane, T. P., and Jakob, C.: Gravity wave influences on mesoscale divergence: An observational case study, Geophys. Res.
Lett., 47, e2019GL086 539, https://doi.org/10.1029/2019GL086539, 2020a.

Stephan, C. C., Schnitt, S., Schulz, H., Bellenger, H., de Szoeke, S. P., Acquistapace, C., Baier, K., Dauhut, T., Laxenaire, R., Morfa-Avalos,
Y., Person, R., Quiñones Meléndez, E., Bagheri, G., Böck, T., Daley, A., Güttler, J., Helfer, K. C., Los, S. A., Neuberger, A., Röttenbacher,
410 J., Raeke, A., Ringel, M., Ritschel, M., Sadoulet, P., Schirmacher, I., Stolla, M. K., Wright, E., Charpentier, B., Doerenbecher, A., Wilson,
R., Jansen, F., Kinne, S., Reverdin, G., Speich, S., Bony, S., and Stevens, B.: Ship- and island-based atmospheric soundings from the
2020 EUREC[4]A field campaign, Earth Sys. Sci. Data Disc., 2020, 1–35, https://doi.org/10.5194/essd-2020-174, https://essd.copernicus.
org/preprints/essd-2020-174/, 2020b.

Stevens et al., B.: EUREC4A, Advances, under review, preprint:https://www.essoar.org/pdfjs/10.1002/essoar.10504890.1, 2020.

415 Stockwell, R. G., Mansinha, L., and Lowe, R. P.: Localization of the complex spectrum: the S transform, IEEE Transactions on Signal
Processing, 44, 998–1001, https://doi.org/10.1109/78.492555, 1996.

van der Dussen, J. J., de Roode, S. R., and Siebesma, A. P.: How large-scale subsidence affects stratocumulus transitions, Atmos. Chem.
Phys., 16, 691–701, https://doi.org/10.5194/acp-16-691-2016, 2016.

Vogel, R., Bony, S., and Stevens, B.: Estimating the shallow convective mass flux from the subcloud-layer mass budget, J. Atmos. Sci., 77,
420   1559–1574, https://doi.org/10.1175/JAS-D-19-0135.1, 2020.

Žagar, N., Kasahara, A., Terasaki, K., Tribbia, J., and Tanaka, H.: Normal-mode function representation of global 3D datasets: open-access
        software for the atmospheric research community, Geosci. Model Dev., 8, 1169–1195, https://doi.org/10.5194/gmd-8-1169-2015, 2015.

Wood, R. and Hartmann, D. L.: Spatial variability of liquid water path in marine low cloud: The importance of mesoscale cellular convection,
        J. Climate, 19, 1748–1764, https://doi.org/10.1175/JCLI3702.1, 2006.

425   Zängl, G., Reinert, D., Ripodas, P., and Baldauf, M.: The ICON (ICOsahedral Non-hydrostatic) modelling framework of DWD and MPI-M:
        Description of the non-hydrostatic dynamical core, Quart. J. Roy. Meteor. Soc., 141, 563–579, https://doi.org/10.1002/qj.2378, 2015.
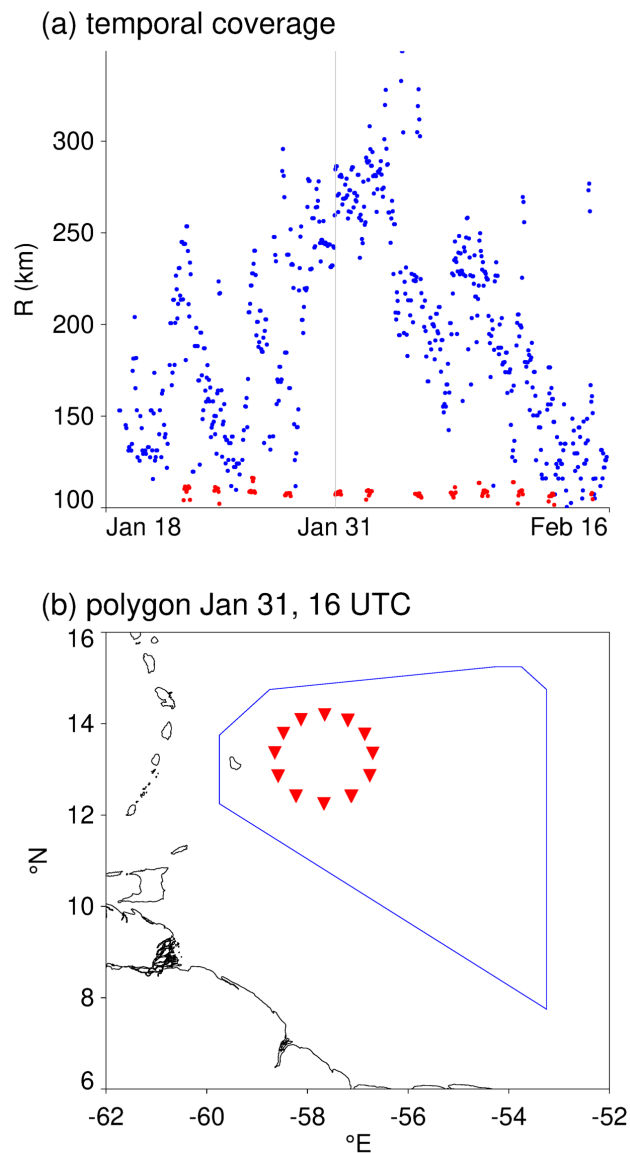
Figure 1. (a) Equivalent radius of the areas sampled by the sounding network (blue) and the HALO circles (red) over the period of the campaign. All points fulfill $L/R < 2$ (see the text for details). (b) For Jan 31, 2020, at 1600 UTC an example of a polygon spanned by radiosoundings (blue) and the location of dropsondes from the HALO circle (red).
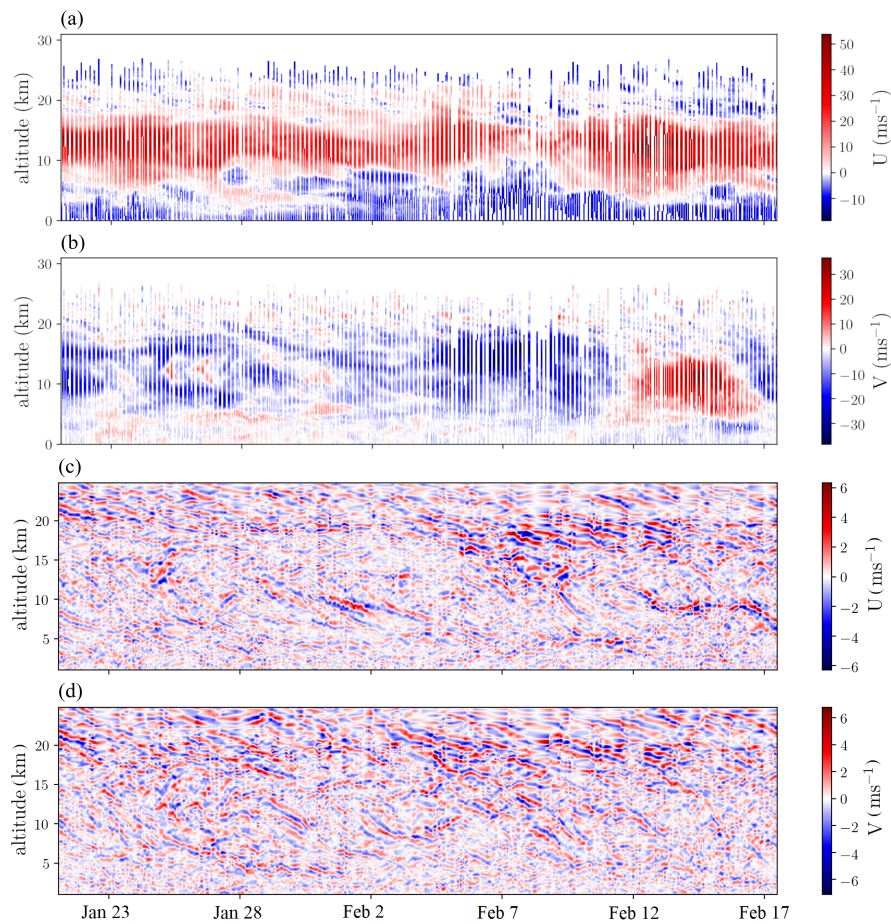
Figure 2. (a) Zonal and (b) meridional wind measured by ascending and descending soundings at the BCO. (c) Zonal and (d) meridional wind perturbations after filtering the raw measurements to 500 m $< \lambda_z <$ 10 km and 3 h $< \tau <$ 53 h.
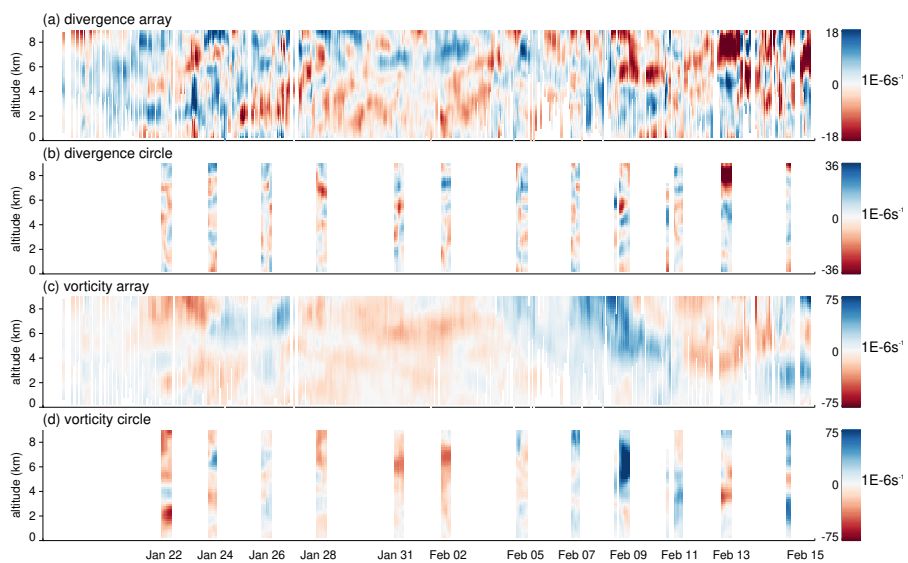
Figure 3. (a),(b) Divergence and (c),(d) vorticity anomalies derived from 3D-Var applied to (a),(c) the sounding network and (b),(d) the HALO circles.
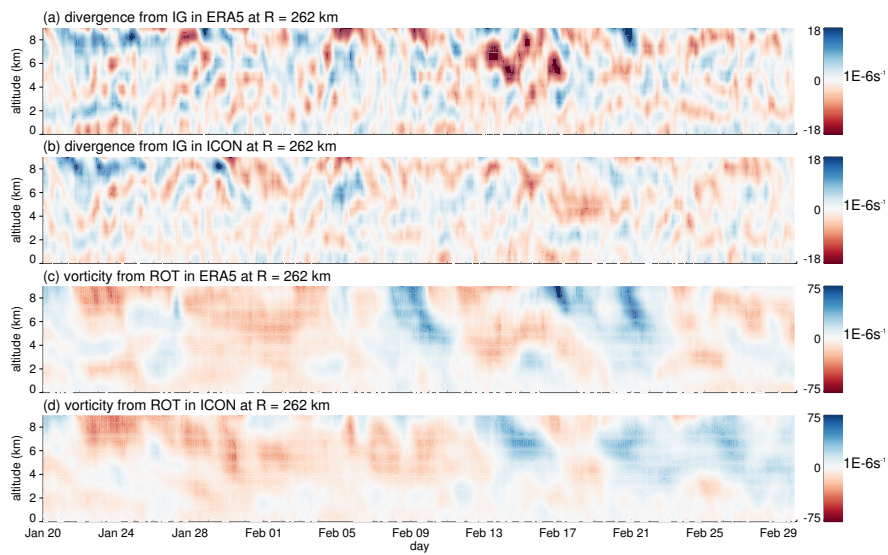
Figure 4. (a),(b) Divergence and (c),(d) vorticity anomalies associated with (a),(b) IG and (c),(d) ROT modes in (a),(c) ERA5 and (b),(d) ICON for an equivalent radius of 262 km. The area is centered on ~12° N, -57° E, matching the approximate location of the EUREC[4]A sounding network (compare Fig. 1b).
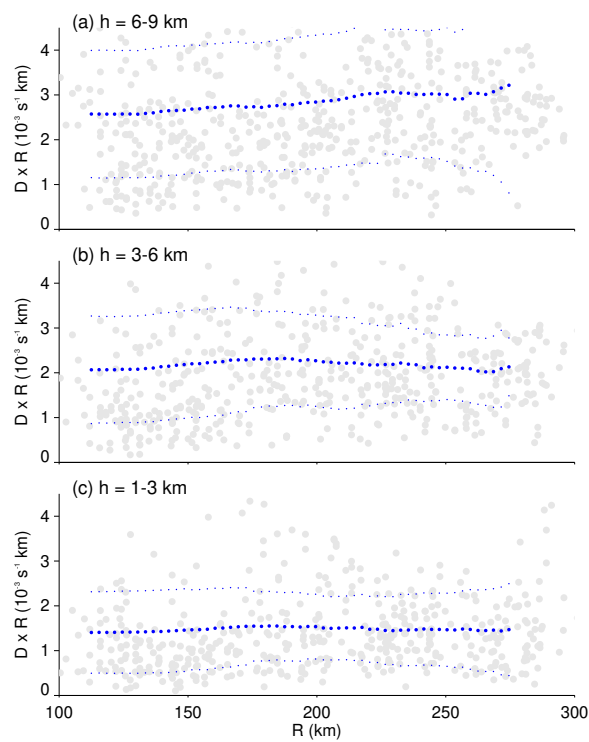
Figure 5. Divergence amplitude anomaly (defined as maximum minus minimum at (a) 6–9 km, (b) 3–6 km, (c) 1–3 km altitude) multiplied by equivalent radius, as a function of equivalent radius. Based on divergence from 3D-Var applied to the sounding network. Thick (thin) blue dots show the running mean ($\pm$ one standard deviation), using R- intervals of 25 km.
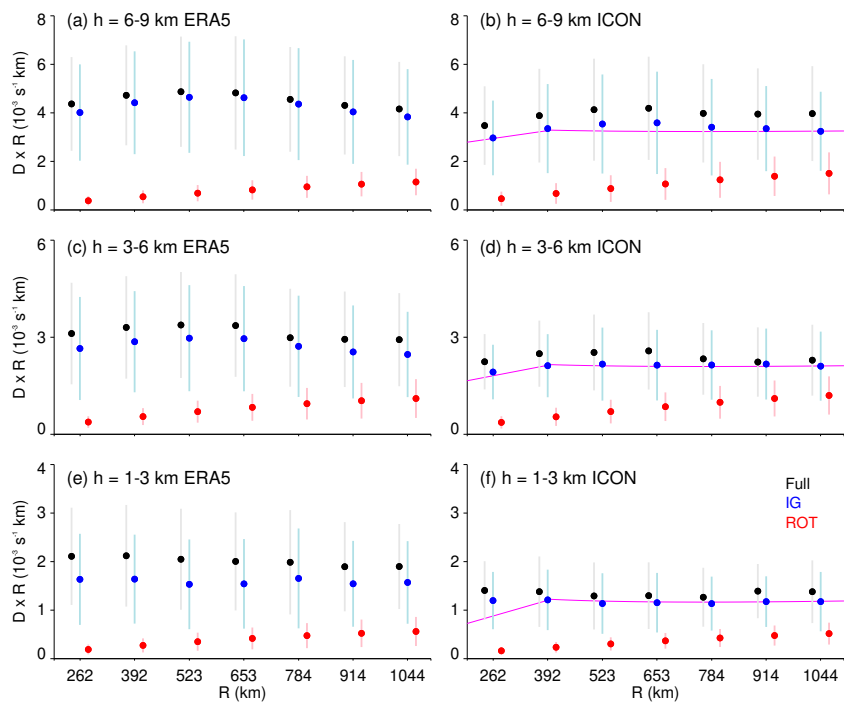
Figure 6. Divergence amplitude anomaly (defined as maximum minus minimum at (a) 6–9 km, (b) 3–6 km, (c) 1–3 km altitude) in (a),(c),(d) ERA5 and (b),(d),(f) ICON. The vertical lines mark ± one standard deviation.
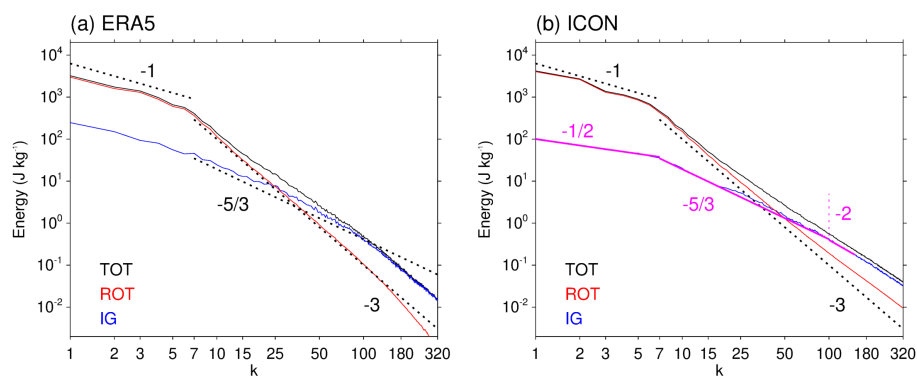
Figure 7. (a),(b) Energy spectra as a function of zonal wavenumber from MODES applied to (a) ERA5 and (b) ICON. The (black) total energy spectrum is decomposed into (red) ROT modes and (blue) IG modes. Dashed black lines show spectral slopes of k^{-1}, $k^{-5/3}$, and k^{-3}; magenta lines in (b) show $k^{-1/2}$, $k^{-5/3}$, and k^{-2}, where the transition between $k^{-5/3}$ and k^{-2} is at $k = 100$ and marked by a thin vertical magenta line.
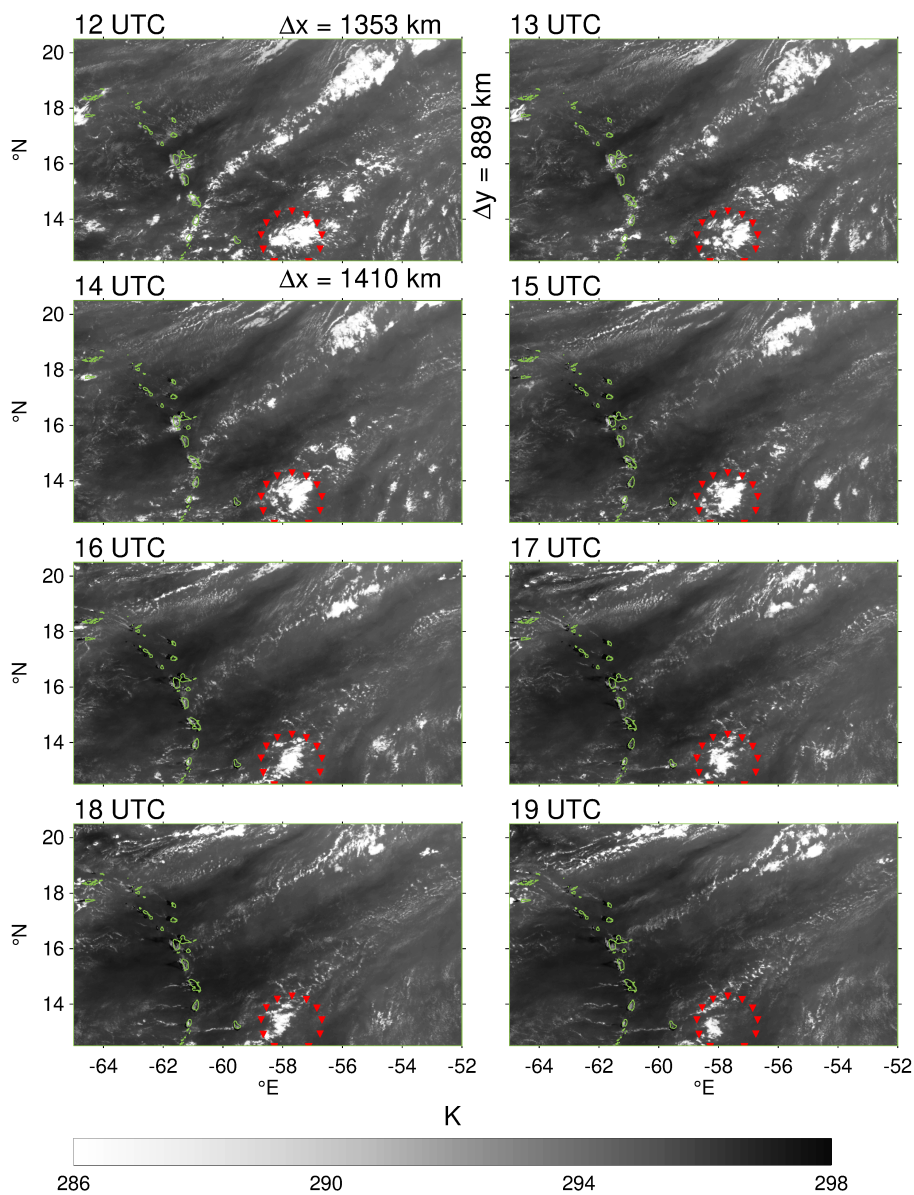
Figure 8. GOES-16 images from Jan 31, 2020, on a regular longitude and latitude grid. The top edge of the images measures 1358 km, the bottom edge 1410 km, and the sides 889 km. Shown are brightness temperatures from the C13 channel. Green outlines show the Caribbean Islands and red triangles the locations of HALO's dropsondes.

Table 1. For all identified wave events, columns list the (1) time interval as "start-date/start-hour – end-date/end-hour" with hour in UTC, (2) dataset (R: *RH-Brown*, M: *Meteor*, B: BCO, C: Combined), (3) altitude interval used for the computation of Stokes parameters, (4) degree of polarization, (5) wave propagation direction counter-clockwise from the eastward direction computed with the Stokes parameters, (6) wave propagation direction obtained with equation (1), (7) vertical wavelength, (8) horizontal wavelength, (9) intrinsic period, (10) ground-based period obtained from the quadrature spectrum.

t_1–t_2	S	h_1–h_2	d	Θ	$\Theta_{T_{90}}$	λ_z	λ_h	τ^*	τ
day/hour		m		°	°	m	km	h	h
Jan									
14/01–14/-11	R	6000–15710	0.84	15	3	3306	718	29	19
18/15–19/-00	R	4000–15710	0.81	-44	-3	2198	521	30	15
20/21–21/-07	R	6000–13710	0.80	17	-3	1585	274	24	11
21/15–22/07	B	5030–15810	0.86	25	-9	5365	1836	37	21
23/23–24/17	M	6000–11750	0.86	34	-20	1043	103	14	27
25/05–25/19	M	6000–17750	0.80	4	-1	5190	226	7	25
25/08–26/10	B	13020–17810	0.80	18	-23	1848	234	19	41
26/04–26/16	C	6000–17640	0.82	2	1	2502	668	33	19
27/02–27/17	B	1030–13810	0.86	-13	4	4847	430	12	41
27/10–27/19	C	4000–15640	0.81	32	-10	1937	159	12	33
27/21–28/11	M	4000–15750	0.85	-27	9	2845	1561	45	22
28/07–29/02	C	0–17640	0.81	-16	20	3553	126	6	26
29/20–30/05	B	5030–15810	0.86	-4	2	2861	1100	39	19
29/21–31/02	R	8000–17710	0.81	-4	4	2526	861	38	33
31/14–01/00	C	3000–8640	0.85	-25	-2	1749	175	14	50
30/16–31/05	C	10000–17640	0.82	16	0	1596	174	17	50
31/05–01/00	B	7030–13810	0.86	-14	-3	3192	477	22	33
31/14–31/23	M	4000–7750	0.86	-28	-1	2286	339	20	27
31/17–01/02	R	5000–9710	0.87	-11	4	3962	441	16	34
Feb									
01/01–01/16	M	6000–13750	0.85	0	-0.63	1302	120	14	19
01/22–02/12	B	3030–13810	0.86	20	-15	1279	68	8	36
02/20–03/07	C	5000–11000	0.85	-27	10	1944	138	10	41
01/07–02/06	R	4000–13710	0.80	-24	-7	2987	536	24	31
05/03–05/15	C	4000–11000	0.85	-15	-5	993	179	24	39
05/11–05/20	R	1000–10710	0.86	-33	-3	815	64	12	44
05/14–06/11	B	4030–7000	0.86	22	7	1062	191	23	22
05/12–05/22	M	0–3750	0.86	-12	-4	2435	111	8	16
07/05–07/17	C	0–17640	0.80	-41	10	1882	80	7	18
07/18–08/08	R	0–11710	0.80	28	6	4264	565	21	29
08/08–09/03	B	903–15810	0.85	0	5	6964	1395	27	33
08/21–09/09	R	6000–15710	0.82	21	-4	2895	417	21	15
09/13–10/04	B	5030–11810	0.85	-30	-7	2776	638	29	29
11/09–11/21	M	6000–13750	0.85	-41	0	775	41	8	12
15/17–16/07	B	13030–17810	0.86	27	9	3179	711	28	31
Average			0.84	-3	0	2645	461	21	28
Stddev			0.02	23	9	1434	445	10	11